Nano-CT scans in the optimisation of purposeful experimental procedures: a study on metallic fibre networks.

Wolfram A. Bosbach*

University of Cambridge, Engineering Department, Cambridge CB2 1PZ, UK

Abstract

Motive Metallic fibre networks and their mechanical behaviour are only insufficiently understood. In this particular field of research, the use of nano-CT scans offers advanced opportunities for the optimised planning of experimental work and component design. Several novel applications will benefit from this research; in particular, tissue engineering applications where a controlled and reproducible mechanical stimulus on cells is required can make use of these components. **Method** For the present study, the geometry of metallic fibre network samples is measured and digitalised through the use of nano-CT scan protocols and adequate radiological post-processing steps. Fibre medial axes are transferred into finite element assemblies and are exposed to magnetic actuation models. Network displacement of input geometries is quantified by averaging of node displacement fields. **Key results** Complex 3D deformation fields with regions of tension, shear, and compression are obtained. Results from a previous study about matrix material deformation can be confirmed in this study for greater sample geometries. The strain magnitude is not uniform across the samples; several influencing parameters and deformation patterns are identified. A simple analytical model can be presented which quantifies the material deformation. **Conclusions** Nano-CT scans provide an efficient radiological tool in the planning of relevant experimental procedures. The present study confirms the general usability of fibre networks for the contactless creation of 3D strain fields in tissue engineering. Mechanical effects in tissue growth stimulation known from experimental work are obtained numerically for the investigated assemblies. Further work about the mechanical effects in tissue cultures appears highly worthwhile.

Word count

Words in text: 5399, Words in headers: 45, Words outside text (captions, etc.): 196
(by https://app.uio.no/ifi/texcount/online.php)

Introduction

Motivation. Today's existing knowledge about the mechanics of fibre networks can be considered incomplete. The present study wants to make a contribution to that field and apply nano computed tomography (CT) [1]. It uses nano-CT image acquisition and image processing in the context of optimising purposeful experimental work and component design. Together with experimentally validated finite element (FE) simulations, the deformation of ferromagnetic fibre networks under magnetic actuation is investigated numerically. Previous studies have estimated the deformation on global level [2, 3], they relied on simplified single-fibre geometries [4], or they investigated a reduced sample volume in interaction with matrix materials [5]. The presented results now are for real fibre network geometries obtained by nano-CT scans. Distinct deformation patterns in the material are discovered under magnetic actuation. This study was part of a dissertation project at the University of Cambridge [6].

Material types and the role of geometric input data. The field of metallic fibre networks has attracted a lot of research attention but many unknowns remain to be solved. The mechanics, as well as the architectural patterns, of sintered fibre networks, as used for the present study, have been investigated experimentally and numerically [7, 8, 9, 10, 6]. Beam theory offers an elegant simplification for computational, cheap simulation of fibre networks under mechanical or magnetic actuation [10, 5]. A magnetic actuation model for ferromagnetic fibre networks has been proposed and applied [4, 5]. The role of computational physics and the FE method is very important in this context. Numerical studies allow resource efficient ex-ante predictions about potential new experiments or they can provide investigations of experimentally highly expensive aspects, such as the micro behaviour within the fibre network structure. Precision of numerical study output heavily relies on the quality of input data. This includes 3D specimen dimensions. Tomography imaging acquisition based on Roentgen rays plays an increasing role with constantly improving hardware and software which is available [11, 12, 13].

*Corresponding author
Email address: wb248@cantab.net (Wolfram A. Bosbach)

In general, physical properties of interest are the mechanical response [14, 15, 16, 10], magnetic response [17, 2, 3], thermal conductivity [15, 18, 19, 20], or the practical damage behaviour [21, 22, 23]. A wide range of fibre materials has been investigated so far. Polymeric non-woven fabrics have been studied [24, 25, 26]. Actin networks and cytoskeletons are one focus of research in biomaterials [27, 28, 29]. Cellulose material which is the basis for the production of paper has attracted the interest of researchers [30, 31]. A field of its own is that of theoretical materials. In these studies, computationally generated networks are simulated and allow predictions about real world materials [32, 33, 34, 35, 15].

Non-medical engineering applications. Metallic fibre networks with or without sintered inter-fibre bonds have been proposed for various applications. One possible mechanical application would be that of composite reinforcement. A viable concept was shown very early for bioglass [36]. Studies about the reinforcement of the bone-cement mantle (ploymethyl methacrylate) required for cemented orthopaedic prostheses followed [37, 38], bone-cement fracture being one major cause of prosthesis failure. Also their application as filters [39] or heat exchangers [40, 41] has been researched. The results for magnetic actuation in the present study are of great interest because ferromagnetic fibre networks could be controlled contactless for shape changes and make advanced applications possible. For example, the drag imposed on a fluid streaming through the mentioned filters or heat exchangers could be amended. Experiments with cellulose fibres coated with magnetite nanoparticles have shown that advanced paper with inherent magnetic properties can be produced [42, 17]. Advanced paper allows the investigation of novel concepts for security paper or also for data storage.

Medical engineering applications. In medical engineering, fibre networks can be found as biomaterials in nature. The cell's cytoskeleton has been in the early focus of fibre network biomechanical research [43, 44, 45] because of its important role in cell division and cell movement. And fibre networks also play a role in medical engineering as scaffold materials for tissue and organ engineering. Suitable networks can be obtained in various ways of production, such as electro spinning [46]. The material for the present study is produced by fibre mat compression and sintering [6, 8, 9, 10, 5]. For the engineering of tissue, the delivery of a precise and locally focussed mechanical stimulus can be mandatory [47, 48, 49]. Rubin found already in 1985 [50] that at frequencies of 1.0 Hz cyclical strain of the magnitude 0.001 can lead to periosteal and endothelial bone growth which is achievable by the fibre networks investigated here [5]. The healing of bone defects is one of the current topics in tissue engineering [51]. Growth inducing tissue scaffolds are one way to access new therapeutic concepts for enhanced patient benefit. This present study wants to investigate through the application of nano-CT images further for metallic fibre networks the influencing variables of their deformation locally and globally under a magnetic stimulus.

Mathematical notation. The present study uses a mathematical notation as follows. Scalars are written x, vectors $\overline{x}$, and 2^{nd} rank tensors $\overline{\overline{x}}$. Cube faces are written X. The vector product is written as "$\times$" and dot product as "$\cdot$". Relations which are greater-than and approximately equal are given as "$\gtrsim$". The operator for the combination of volumes is given as "$\cup$".

Materials and Methods

For the present study, networks of compressed and sintered steel fibre mats are produced. The geometrical dimensions are obtained through nano-CT scanning [1]. In image post-processing, images are segmented in fibre and air. The fibres are meshed as FE beam assemblies. The mechanics are analysed through application of the FE solver Abaqus [52].

Material production and material phases. Six fibre network sample cubes of volume $V = 4.00^3$ mm^3 (Fig. 1.a) are chosen as material samples for the present study. The fibre material was used before in studies [8, 10, 5]. V consists of two phases, fibre phase V_{fibre} and void phase V_{void}:

$$V = V_{fibre} \cup V_{void} \tag{1}$$

The present study follows a two-phase model [15, 10] for random fibre networks containing a void phase. In this model, the Cauchy stress tensor $\overline{\overline{\sigma}}$ [56] is defined for fibre phase and void phase:

$$\overline{\overline{\sigma}} \neq 0 \;\forall\, \overline{x} \in V_{fibre} \quad , \quad \overline{\overline{\sigma}} = 0 \;\forall\, \overline{x} \in V_{void} \tag{2}$$

Eq. 2 implies that forces or moments can only be prescribed on V_{fibre} (i.e. the steel fibres, not the void inter-fibre space). The volume surface S is defined to consist of six quadratic cube faces, two of them perpendicular each to one of the three axes. Two cube faces, F_x and F_y, are of relevance for the boundary conditions (BC) in the present study (Fig. 1.a, d, e).

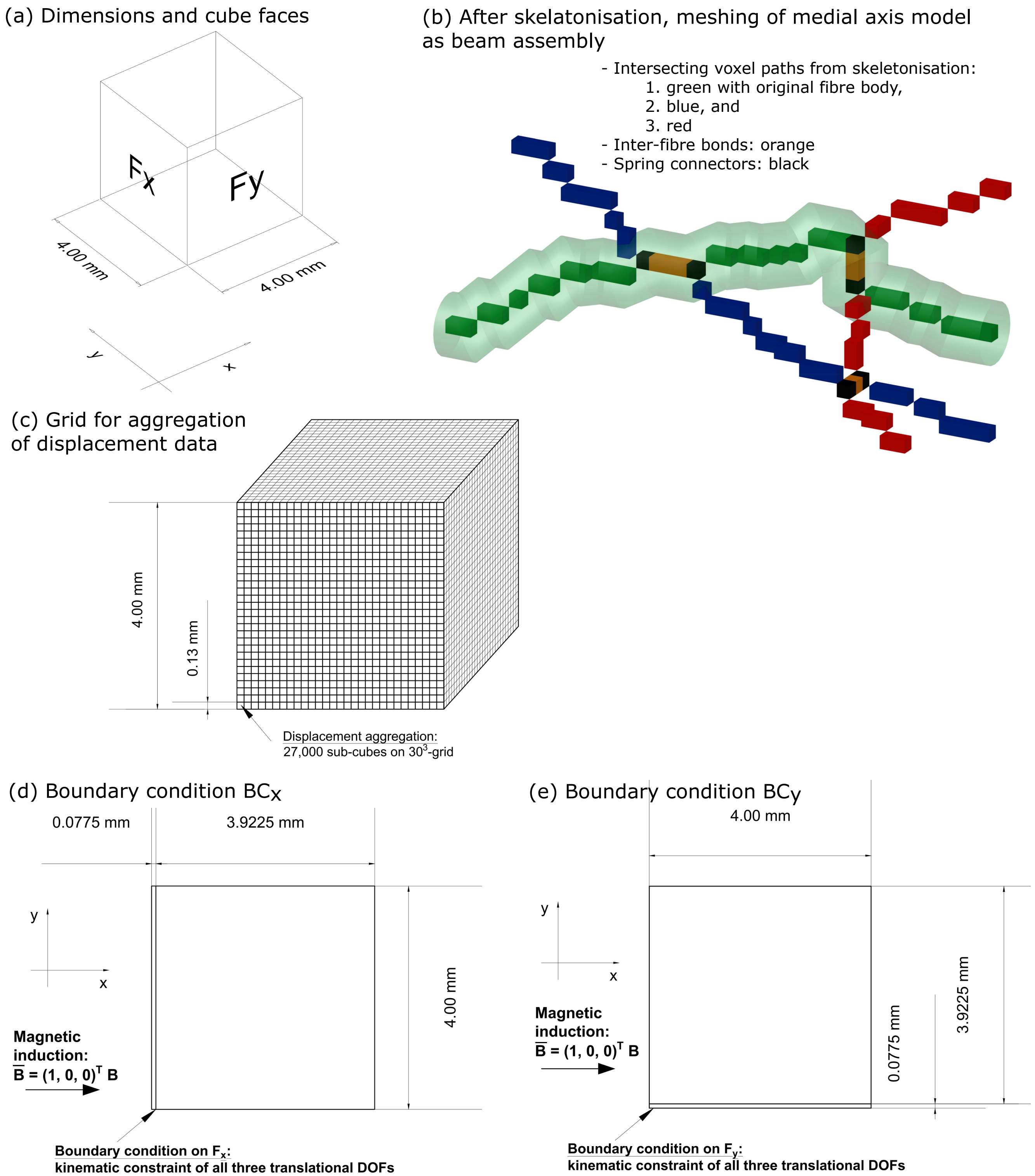

Figure 1: **Material samples:** (a) Sample cube dimensions, (b) meshing of medial axis model after skeletonisation post-processing step [53, 54, 55] as beam assembly, (c) aggregation of displacement data on 30^3-subgrid., (d) and (e) boundary conditions $\mathrm{BC_x}$ and $\mathrm{BC_y}$.

The network material is produced at N.V. Bekaert S.A. (Belgium) as mats by solid state sintering of compressed stacks of austenitic American Iron And Steel Institute (AISI) 316L stainless steel fibres. For the present study, the material is simulated for a hypothetical magnetic saturation M_s as it would be applicable in the case of ferritic AISI 444. It has been shown that the AISI 316L geometries can equally be obtained for ferritic AISI 444 material [8, 9].

This modelling assumption has been applied before to the material of this present study; the AISI 316L geometries are treated in the FE model as if they were AISI 444 [5]. The study's sample cubes (Table 1) are cut by electronic discharge machining (EDM). Two of the sample cubes are produced each for a fibre density f of 10, 15, or 20%.

Nano-CT scanning and image post-processing. Nano-CT scans are acquired at General Electric (Germany) for a resolution $R = 7.75\,\mu m$ (voltage $U = 120\,kV$, current $I = 40\,\mu A$, 360° with step size 0.25°). The machine uses sub-micron focal spot technology and a copper-0.2 mm filter [1]. Greater R is obtainable by nano-CT but reduces the obtainable scanner volume V. The sample scans are segmented (V_{fibre}, V_{void}) and reduced to their medial axes (i.e. voxel paths) through application of a skeletonisation post-processing algorithm (Fig. 1.b) [53, 54, 55]. Architectural along with mechanical characterisations of the material in Table 1 have been published [8, 10]. For the mechanics of the material it is of importance that with greater material density, i.e. f, the average segment length λ between two sintered joints decreases. Greater beam bending stiffness is the consequence.

Table 1: **Fibre network samples:** Skeletonisation and FE meshing, network node distribution.

Sample	**CT scan skeletonisation**		**Number of meshed elements**			**Singularities**	
	Fibre segments	λ [µm]	Network nodes	B31/B32	CONN3D2	$\mathbf{BC_x}$	$\mathbf{BC_y}$
10%-No.1	22,913	235	738,317	700,515	50,960	5	4
10%-No.2	22,789	239	747,015	709,427	50,582	2	4
15%-No.1	37,049	191	993,772	929,249	87,708	2	1
15%-No.2	41,479	181	1,109,687	1,029,453	109,364	-	-
20%-No.1	59,936	153	1,382,385	1,265,910	159,257	-	-
20%-No.2	59,949	153	1,386,398	1,269,925	159,246	1	1

Sample	**Network nodes**	**Median**			**Rel. Std. Deviation**		
	Average per 2D pixel slice	x-axis	y-axis	z-axis	x-axis	y-axis	z-axis
10%-No.1	1,431	1,440	1,434	1,424	8.61%	8.48%	12.75%
10%-No.2	1,448	1,443	1,436	1,439	7.99%	8.36%	13.04%
15%-No.1	1,926	1,920	1,931	1,918	7.34%	7.05%	9.48%
15%-No.2	2,151	2,150	2,139	2,140	7.02%	7.13%	9.10%
20%-No.1	2,679	2,683	2,675	2,678	6.11%	6.81%	8.62%
20%-No.2	2,687	2,683	2,667	2,686	6.66%	7.39%	8.13%

The medial axis models are transferred into beam assemblies for the FE solver Abaqus 6.12 and 6.13 [52]. One Timoshenko beam [57, 58, 59] of linear interpolation (B31, Table 2) and one of quadratic interpolation (B32) is implemented. The beams are simulated for a simplified round cross section of diameter $d = 40\,\mu m$ (i.e. cross section area $A = (d/2)^2\pi$), a Young's modulus of $E = 200\,GPa$, and for a Poisson's ratio of $\nu = 0.3$. The inter-fibre network joints obtained in the sintering step, dividing fibres into fibre segments, are connected to the network by torsional springs (CONN3D2). For the present study, the CONN3D2 stiffness is set to $K_{joint} = s\,E\,A$. s is used as scaling factor (Table 2). This joint modelling allows for the directed variation of the simulated joint stiffness. It is known that for values $s > 3,000$ µm the network's E approximates that obtained for rigid joints. An experimental validation of the network E is obtained for $s = 5$ µm. s has a non-linear influence on the network's mechanical response and is discussed in Fig. 4 and Eq. 9, 10 at the end of the results chapter [10].

Table 2: **Model implementation:** Abaqus element types [52] and simulated parameter values.

Element Type	**Identifier**	**Geometry**	**Interpolation/Connection**
Spring connector	CONN3D2	3D	join & torsional spring
Timoshenko beam	B31	3D	linear interpolation
	B32	3D	quadratic interpolation

BC	**Beam**	**Scaling factor *s*** [µm]	**Magnetic induction *B*** [T]
BC_x	B31	5	0.25
BC_y	B32	10	0.50
(Fig. 1)		30	1.00
		300	2.00

Table 1 contains further information about the size of the FE meshes. The number of meshed elements (beams and springs) increases for greater f. All network nodes are located first inside V, and second due to the CT scan resolution R on a $[516\,R]^3$-grid.

FE model of magnetic actuation. Two different BC settings are implemented (Fig. 1.d, e). At the time of the study's design, this assembly of in-plane magnetic actuation was subject to on-going experiments at the University of Cambridge. In both cases, a magnetic induction vector $\overline{B} = [1, 0, 0]^T B$ along the x-axis is simulated. For BC_x (BC_y), all beam elements located on the cube face F_x (F_y) are constrained kinematically along all three translational degrees of freedom (DOF) to a depth of $h_{BC} = 77.50\,\mu\text{m}$ into the material. The value of h_{BC} is the equivalent of 10 pixels in the CT scans. It was chosen for the present study as it was found to approximate the stiffness magnitude of experimental in-plane tensile testing [8, 10].

Under the assumption of complete magnetisation for a hypothetical saturation value of $M_s = 1.6\,\text{MA/m}$, a moment vector $\overline{\tau}$ is imposed on every beam element. The modelling approach has been applied before to the material under magnetic actuation [5]. This value of M_s is validated for ferritic AISI 444 in an experimental measurement which can be found in [4]. As mentioned above, the meshed geometries of Table 1 were obtained for austenitic AISI 316L. For this study, it is part of the modelling assumptions that the network is simulated for the hypothetical M_s of AISI 444. The networks are treated as if they were manufactured from AISI 444 which is equally possible [8, 9]. $\overline{\tau}$ is obtained as $\overline{\tau} = \overline{m_{tot}} \times \overline{B}$. The total magnetisation per beam element depends on fibre volume and fibre orientation: $\overline{m_{tot}} = \overline{M_s} A_{fibre} L$; being aligned to the beam axis [4].

The system is solved in this study for the imposed BC under the assumptions of linear elasticity and respecting the equilibrium conditions of forces and moments. The unit outward normal and $\overline{\overline{\sigma}}$ define the surface traction vector: $\overline{t} = \overline{\overline{\sigma}} \cdot \overline{n}^{out}$. Body force per volume $\overline{f}$ is neglected in the present study ($= 0$); gravitational forces being a typical example for $\overline{f}$. This implies that the general form for the equilibrium of forces [60] in Eq. 3 can be simplified for the present study to the form in Eq. 4.

$$\int_S \overline{t}\ dS + \int_V \overline{f}\ dV = 0 \tag{3}$$

$$\text{Eq. 3} \quad \xrightarrow{\overline{f}=0} \quad \int_S \overline{t}\ dS = 0 \tag{4}$$

The equilibrium of moments [60] in Eq. 5 is calculated with respect to the origin of the point vector $\overline{x}$. The general form can be rewritten to Eq. 6 for the present study, considering $\overline{f} = 0$ and adding the sum of imposed $\overline{\tau}$ as magnetic actuation [5].

$$\int_S (\overline{x} \times \overline{t})\ dS + \int_V (\overline{x} \times \overline{f})\ dV = 0 \tag{5}$$

$$\text{Eq. 5} \quad \xrightarrow{\overline{f}=0,\ +\overline{\tau}} \quad \int_{F_x} (\overline{x} \times \overline{t})\ dS \quad \overbrace{+ \sum_{V_{fibre}} \overline{\tau}}^{\text{magnetic actuation}} = 0 \tag{6}$$

The relevant section of S is defined by the simulated BC, i.e. cube face F_x or F_y (Fig. 1.d, e). Eq. 3 to 6 adopt the Lagrangian reference frame [61]. The Eulerian reference frame [62, 63] is advantageous for the modelling of fluids. The analyses of the present study are run on a local workstation. This workstation has two Intel(R) Xeon(R) X5650 CPU processors (2.66 GHz, 6 threads and 12 cores each) with an available memory of 96 GB-RAM. For the implemented model, the solver runs into up to five singularities (Table 1). These are caused by fibre segments which are mechanically unconnected to the rest of the mesh. Due to the mesh size ($\approx 10^6$ network nodes), this number of singularities is negligible for the mechanical analyses of this study. For the facilitation of the solving process, all six DOF are constrained on these nodes.

For the evaluation of the obtained displacement field defined on the 516^3-grid, it is aggregated on a 30^3-subgrid (Fig. 1.c). First, the obtained results of node displacement are averaged per grid cell. Second, the equivalent von-Mises strain $\varepsilon_{v.M.}$ is calculated from this for each grid cell [64, 65].

Results

The results of this study analyse the network geometries as obtained in nano-CT post-processing for its mechanical response under magnetic actuation. Distinctive, reproducible patterns of local deformation and strain distribution are discovered in the material. These are discussed here, also with regard to the material density distribution inside the samples. These findings are of importance with regard to the medical applications in tissue engineering where the magnitude of mechanical strain is decisive [50] .

Material density distribution. Due to the statistical nature of the investigated network material, the study of sample geometry with regard to density and isotropy of fibre orientation is mandatory for mechanical analysis. The samples are analysed in Table 1 and Fig. 2 for the exhibited material density as obtained for the given V. This material property, together with the fibre orientation distribution, is of great relevance for the conclusions from the deformation patterns presented in the following sections. From previous architectural analyses [8, 9], it is already known that the main orientation direction of fibre segments lies parallel to the xy-plane. Yet in the xy-plane itself, no dominating direction of fibre orientation exists.

The post-processed [53, 10] nano-CT scans are the described strings of voxel cubes. Table 1 contains for each sample the average number of FE network nodes per 2D pixel slice in the sample cube. Their absolute number of 0.7 million ($f = 10\%$) to 1.4 million ($f = 20\%$) per sample leads to a numerical average number of nodes between 1.4 thousand and 2.7 thousand for each 2D pixel slice along each of the three axes. The median found for their distribution is shown in Table 1 too. It shows that the distribution median of network nodes per 2D pixel slice deviates in the investigated samples only marginally from the numerical average value. This holds true for each sample along each of the three axes. The obtained relative standard deviation expressed as ratio of the mean amounts to less than 8.6% in-plane and 13.0% out-of-plane. These numbers show that the in-plane deviation is generally less than the out-of-plane one along the z-axis. This observation concerning material density is new and is of great interest for future manufacturing tolerance measures. Of interest is also that the obtained standard deviation decreases for greater f. This trend implies for greater f a more even fibre distribution during manufacturing.

In addition to Table 1, Fig. 2 plots the distribution of network nodes per 2D pixel slice along the three axes for each sample. The total network nodes are plotted for a 129^3-grid when counted per grid cell along the three axes. As shown by the median and standard deviation in Table 1, a deviation from the numerical average exists; however, specific regions of greater/lesser density don't. The greatest deviation from the sample average is obtained in each case at the cube faces. The cube faces are obtained after sintering of the compressed fibres and after the cutting by EDM. This analysis demonstrates that these two manufacturing steps also will need to be considered further in the future by tolerance measures.

These findings of a uniform distribution in the given sample size ($V = 4.00^3$ mm^3) are of importance for the deformation patterns discovered in the material under magnetic actuation. The deformation patterns are not caused by non-uniform material density or fibre orientation in the sample cubes. Instead, they can be seen as an inherent and reproducible material feature exhibited by this statistical network.

Deformation patterns and deformation magnitude. The parameter values simulated in the present study for s and B are shown in Table 2. Each parameter value is simulated in combination with all others. This means that 64 simulations are run for each of the 6 samples.

Fig. 3 exhibits distinct so far unknown deformation patterns. Those patterns are of great interest with regard to the discussed potential applications of the material. The displacement plots of Sample-15%-No.1 under magnetic actuation of $B = 0.50\,\mathrm{T}$ are plotted for both BC. u [µm] is plotted together with its components along the three axes u_1, u_2, u_3. Although the network's architecture has been known before, its precise deformation under magnetic actuation wasn't. Now, it can be seen that the network is exposed to a complex 3D deformation state. A summary of the deformation types is given in Table 3. This complex 3D deformation is in contrast to the very uniform elongation found for this network type under uniaxial mechanical actuation [10].

Table 3: **Deformation type:** Elongation, compression, and shear under magnetic actuation and resulting deformation patterns (Fig. 3).

Deformation	$\mathbf{BC_x}$	$\mathbf{BC_y}$
Elongation	u_1 - red	u_2 - red
Compression	u_1 - blue	u_2 - blue
Shear	u_2 - blue	u_1 - red

Displacement	$\mathbf{BC_x}$		$\mathbf{BC_y}$	**Obtained deformation pattern**
Total	$\overline{u}$	$\leftrightarrow$	$\overline{u}$	rings of half circles
In-plane	u_1	$\leftrightarrow$	u_2	max and min value in opposing corners on cube face opposing BC
	u_2	$\leftrightarrow$	u_1	"cantilever beam bending"
Out-of-plane	u_3	$\nleftrightarrow$	u_3	-

In the network, regions of tension and compression (u_1 for $\mathrm{BC_x}$, u_2 for $\mathrm{BC_y}$), and also shear parallel to the

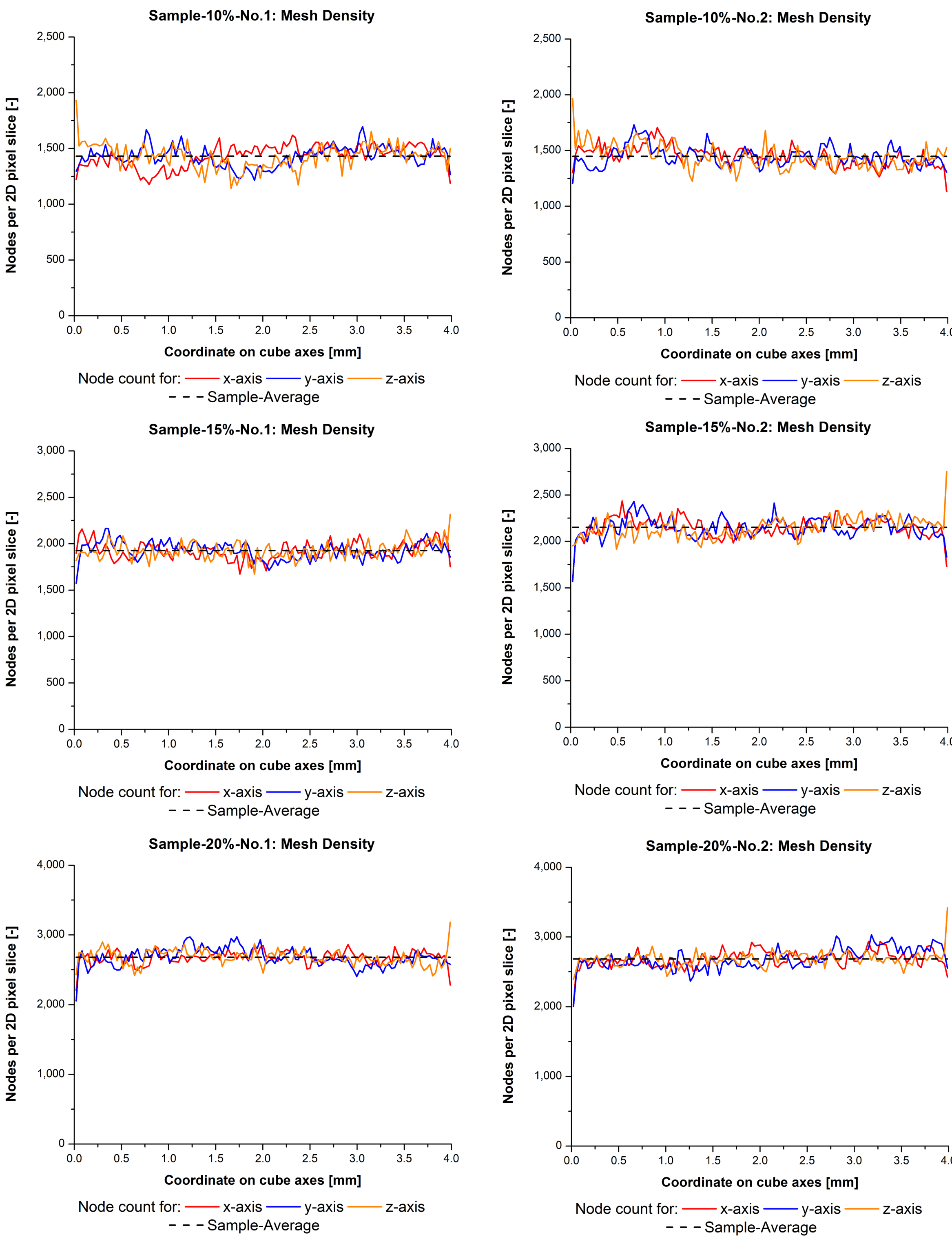

Figure 2: **Material density:** Distribution of network nodes along cube axes.

constrained cube face (u_2 for $\mathrm{BC_x}$, u_1 for $\mathrm{BC_x}$) exist. These are particularly well visible on the cube face opposite to the one constrained under the applied BC. A summary of the observable patters is contained in Table 3. It can be seen for Sample-15%-No.1 in Fig. 3 that on S fibres exposed to great deflection exist which are only loosely connected to the main mesh. The loose connection of these fibres is caused by the EDM cutting process of the sample cubes.

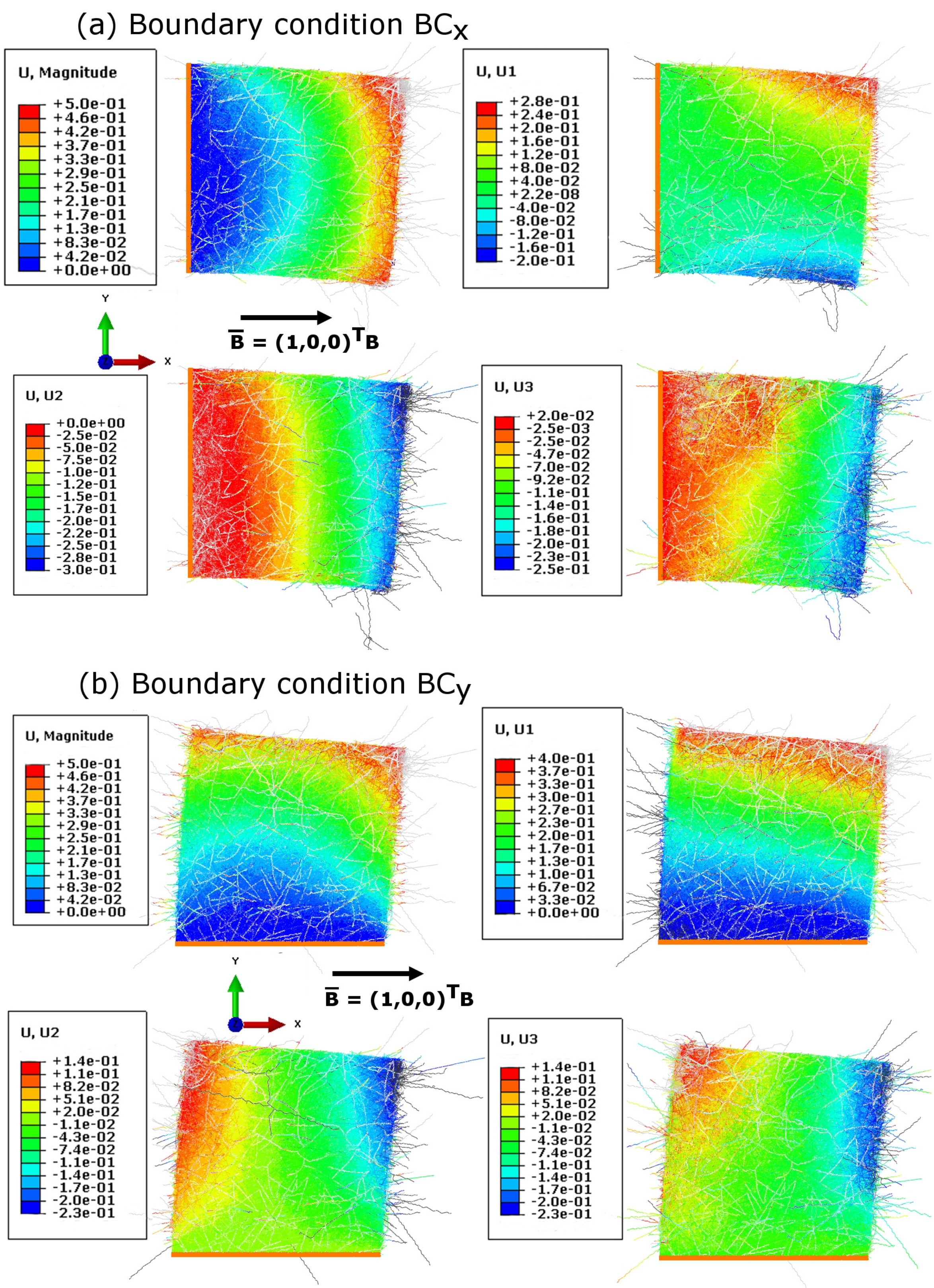

Figure 3: **Deformation plot:** Displacement field $\overline{u}$ and its axial components [µm] under (a) BC_x, and (b) BC_y for Sample-15%-No.1 under magnetic actuation of $B = 0.50\,T$, $s = 5\,µm$, B31.

The patterns obtained for BC_x and BC_y are highly similar relative to the constrained cube face but they are not entirely identical. The total displacement field $\overline{u}$ can be described in both cases by rings of half-circles which are centred on the midpoint of the constrained cube face. The value of u increases for greater circle radius. The patterns for $\mathrm{BC_x}$ and $\mathrm{BC_y}$ obtained for the two in-plane components, u_1 and u_2, match each other. However, they are rotated by 90° just as the constrained cube face. The displacement parallel to the constrained cube face is interestingly similar to that of the bending of a cantilever beam. The displacement perpendicular to the constrained cube face exhibits for both BC a global maximum as well as a global minimum on the cube face opposite of F_x or F_y. The rotation of 90° for the patterns of u_1 and u_2 for the two BC (which are themselves rotated by 90°) matches the observation that no dominating direction of fibre orientation exists in the xy-plane. The deformation along the out-of-plane direction, u_3, shows for both BC a global maximum and global minimum in one of the cube's corners. A pattern comparable for both BC of u_3 is not obtained. It is important to put these results in perspective with the findings about the uniform density distribution in the samples of Fig. 2. The observable patterns are not the result of an uneven density distribution in the samples. Instead, these deformation patterns under magnetic actuation can be considered a reproducible material feature.

In a further step, the displacement fields are averaged on the 30^3-subgrid (Fig. 1.c) and used as input for the calculation of the strain field. This allows for the first time the quantification of the strain obtained under magnetic actuation for the investigated material: the equivalent von-Mises strain measure $\varepsilon_{v.M.}$ is calculated, and averaged for the entire sample (Fig. 4.a, b). For increased accuracy of the plot, the value of f plotted is the one measured by a volumetric measurement technique (sample weight and dimensions) [8].

For a magnetic induction of 0.50 T, the magnitude of $\varepsilon_{v.M.}$ lies within a range from 10^{-4} to 10^{-3} for both BC. $\varepsilon_{v.M.}$ decreases for greater f. In a previous study about the strain imposed under magnetic actuation on a matrix material in the void phase for a sample cube of $V_{red} = 0.775^3\ \mathrm{mm}^3$, a positive $d\varepsilon_{v.M.}/df$ is obtained irrespectively of the matrix stiffness [5, 6]. The change of sample cube size ($V = 4.00^3\ \mathrm{mm}^3 > V_{red}$) results in a size effect regarding network stiffness. Depending on the applied BC, the size effect can increase or equally decrease the network stiffness ($dE/dV \gtrless 0$) [10, 6]. It is one of the interesting features of this material and subject of on-going research.

Because of the linearity assumption, B scales the obtained $\varepsilon_{v.M.}$ linearly (Eq. 6). For the linear or quadratic interpolation of the Timoshenko beams (B31 or B32), a change in obtained $\varepsilon_{v.M.}$ is measurable (Table 4, Eq. 8). The graph (Fig. 4.a, b) demonstrates however that the influence of the linear or quadratic interpolation for the Timoshenko beams can be regarded as negligible for practical considerations. Given the inherent error size arising from other process steps such as the CT scanning or skeletonisation, the difference from beam interpolation vanishes and could well be neglected in later studies about prototype design for the mentioned applications.

Statistical and spatial strain distribution. For the application of a controllable strain field on the cells attaching to a scaffold detailed knowledge about strain size and strain distribution is necessary. Fig. 4.c, d and 5 investigate the strain distribution inside the samples. The results are averaged for the two samples per value of f.

First, the statistical distribution $p_{(x)}$ is shown in Fig. 4.c, d for both BC. Again, the BC has no influence on the overall obtained results. For each distribution curve, one single global peak of $p_{(x)}$ is obtained. It can be seen in each case that for greater f the single global peak of $p_{(x)}$ is shifted leftwards and towards greater values. That shift of $p_{(x)}$ (leftwards and upwards) is also seen when B is changed from 2.00 to 0.25 T. This is in line with $d\varepsilon_{v.M.}/df < 0$ (Fig. 4.a, b) and the linearity assumption towards B (Eq. 6). In the investigated samples, the $p_{(x)}$-peak lies in a range between 0 and 10^{-3} of $\varepsilon_{v.M.}$ for the applied B. This quantification of statistical strain occurrences has been seen before and will also be of great interest for future prototype studies.

Second, the spatial distribution of $\varepsilon_{v.M.}$ is shown in Fig. 5 for both BC. The values of $\varepsilon_{v.M.}$ are averaged along the out-of-plane z-axis and plotted on a 4^2-grid. These plots are of importance because they give details about where greater or lesser values of $\varepsilon_{v.M.}$ can be found inside the samples. The observable pattern for the spatial distribution of $\varepsilon_{v.M.}$ is similar to that of $\overline{u}$ shown before in Fig. 3. The lowest observed values of $\varepsilon_{v.M.}$ are located in the proximity of the midpoint on the constrained cube face. Values of $\varepsilon_{v.M.}$ increase with proximity to the non-constrained cube faces. The maxima of $\varepsilon_{v.M.}$ are located in the corners of the cube face opposing the constrained one. The magnitude of these maxima increases for lesser f. Also in the case of the spatial distribution, the two Timoshenko beams produce highly similar results. As mentioned previously for the displacement patterns in Fig. 3, the patterns shown for the spatial distribution of $\varepsilon_{v.M.}$ are not caused by non-uniform mesh density (Fig. 2). This means that they too can be considered to be a reproducible feature of the investigated material. These findings imply that during the design of further experimental set-ups the local variation in fibre scaffold deformation needs to be taken into consideration in the experimental procedures.

Parameter discussion. For the linear-elastic range, the mechanical response of the material is linear with regard to parameters such as E, M_s, and B. Parameters with non-linear influence on $\varepsilon_{v.M.}$ are f, K_{joint}, and the Timoshenko beam type. The most complex single parameter is the fibre density f. It is obtained by the degree of fibre compression during the network manufacturing and is expressed as fraction of the sample's V. Greater fibre compression alters the bending between fibres, increases the number of inter-fibre bonds, and thus decreases the

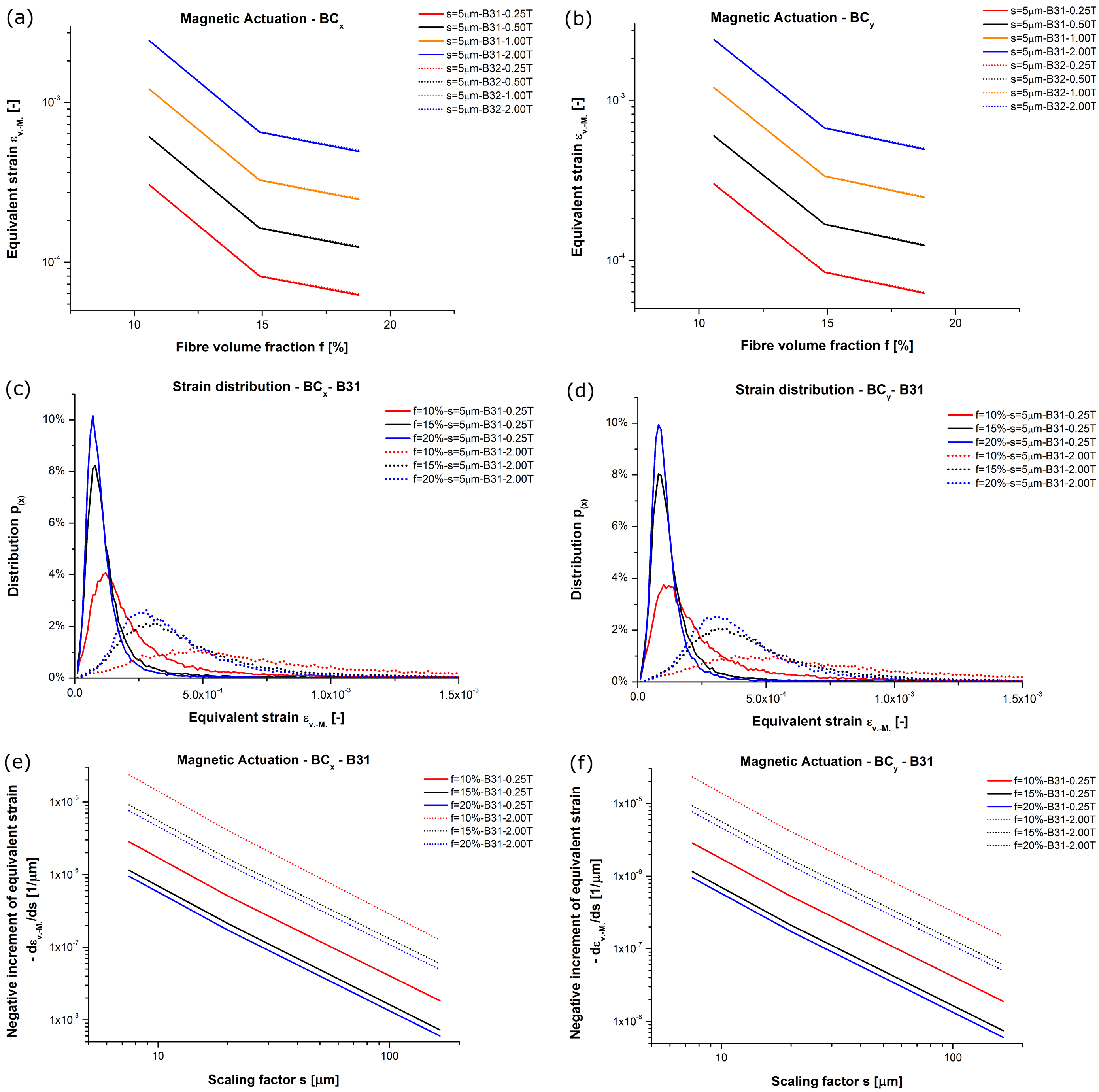

Figure 4: **Strain magnitude:** (a) and (b) obtained averaged $\varepsilon_{v.M.}$ values depending on f, (c) and (d) statistical distribution $p_{(x)}$, (e) and (f) $d\varepsilon_{v.M.}/ds$ in a log-log-plot depending on s, each for $\mathrm{BC_x}$ and $\mathrm{BC_y}$.

fibre segment length λ. The mechanical network response is dominated to a great extent by beam deflection over beam elongation and is strongly affected by a change of f and λ [10]. This is why also for the response to magnetic actuation no simple relationship exists for a change of f. However, it can be seen in Fig. 4.a, b of this present study that $\varepsilon_{v.M.}$ decreases for greater f for the investigated sample volume $V = 4.00^3$ mm^3. The size effect known for the material [10] changes the mechanical response and is also one highly interesting part of the future work. For the two Timoshenko beams (B31 and B32), the mechanical network response is known the be of marginally greater stiffness for B31 (Eq. 7) [10]. The marginally greater E_{B31} would let expect that $\varepsilon_{v.M.}$ conversely increases for B32 when identical magnetic actuation is imposed (Eq. 8). This is confirmed by the results of the present study (Table 4).

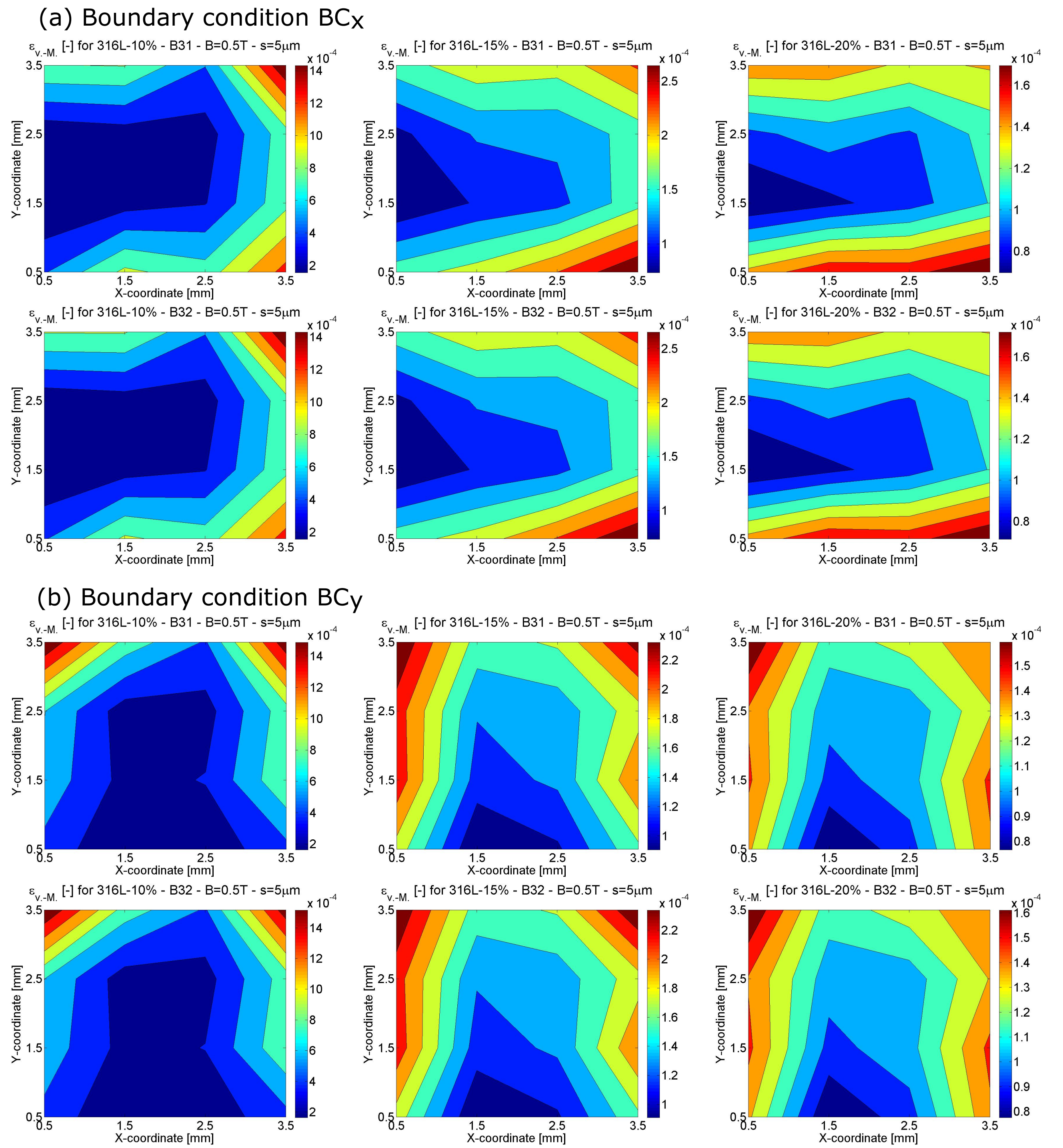

Figure 5: **Spatial distribution:** Obtained local $\varepsilon_{v.M.}$ (averaged for each f and along the z-axis) depending on x and y in (a) for $\mathrm{BC_x}$, and (b) for $\mathrm{BC_y}$.

$$E_{\mathrm{B31}} \gtrsim E_{\mathrm{B32}} \tag{7}$$

$$\varepsilon_{v.M.,\mathrm{B31}} \lesssim \varepsilon_{v.M.,\mathrm{B32}} \tag{8}$$

Independently of the imposed BC, B32 returns marginally greater values for $\varepsilon_{v.M.}$. This holds true for each f, and all combinations of values for s and B, except for one single data point. The magnitude of the deviation is in

Table 4: **Influence of Timoshenko beam (B31 and B32):** $\Delta = \frac{\varepsilon_{v.M.,\mathrm{B32}}}{\varepsilon_{v.M.,\mathrm{B31}}} - 1$.

f=10%	Boundary condition $\mathbf{BC_x}$				Boundary condition $\mathbf{BC_y}$			
s [µm]	$B = 0.25\,\mathrm{T}$	0.50 T	1.00 T	2.00 T	$B = 0.25\,\mathrm{T}$	0.50 T	1.00 T	2.00 T
5	3.97‰	4.04‰	2.87‰	1.25‰	7.88‰	6.35‰	5.41‰	5.20‰
10	3.04‰	3.03‰	5.18‰	4.79‰	7.44‰	6.07‰	5.69‰	5.56‰
30	3.00‰	4.17‰	-2.40‰	4.74‰	7.95‰	6.64‰	5.56‰	5.11‰
300	3.24‰	3.23‰	4.61‰	0.29‰	9.64‰	5.90‰	5.45‰	5.19‰
f=15%	**Boundary condition $\mathbf{BC_x}$**				**Boundary condition $\mathbf{BC_y}$**			
s [µm]	$B = 0.25\,\mathrm{T}$	0.50 T	1.00 T	2.00 T	$B = 0.25\,\mathrm{T}$	0.50 T	1.00 T	2.00 T
5	8.16‰	7.06‰	7.62‰	7.94‰	8.04‰	6.10‰	7.28‰	7.43‰
10	8.08‰	7.61‰	7.66‰	7.82‰	7.83‰	8.02‰	7.38‰	7.68‰
30	9.23‰	8.32‰	8.88‰	8.53‰	8.49‰	7.21‰	9.80‰	8.61‰
300	7.09‰	9.73‰	8.28‰	8.75‰	8.34‰	8.57‰	7.88‰	9.22‰
f=20%	**Boundary condition $\mathbf{BC_x}$**				**Boundary condition $\mathbf{BC_y}$**			
s [µm]	$B = 0.25\,\mathrm{T}$	0.50 T	1.00 T	2.00 T	$B = 0.25\,\mathrm{T}$	0.50 T	1.00 T	2.00 T
5	16.86‰	15.99‰	16.24‰	16.08‰	16.07‰	15.52‰	15.21‰	15.26‰
10	18.10‰	17.28‰	17.21‰	16.92‰	16.50‰	16.08‰	16.06‰	16.10‰
30	19.10‰	17.12‰	17.61‰	17.88‰	17.58‰	16.82‰	17.13‰	16.90‰
300	18.76‰	19.19‰	18.18‰	18.53‰	17.79‰	17.28‰	17.39‰	17.09‰

the range between 3‰ and 2%. With some minor exceptions, an increase of this deviation can be seen for greater f. For practical considerations concerning the applications of the investigated material, this deviation can be seen as negligible. Nonetheless, it is of interest for the accuracy of numerical modelling. The influence of segment length by changing f seems one worthwhile aspect for future research.

The joint stiffness K_{joint}, scaled linearly by s, is known to relate non-linearly to the mechanical response. For ever greater values of s, E tends towards values equal to those of networks with rigid inter-fibre joints [10]. In this study, the influence of s on $\varepsilon_{v.M.}$ under magnetic actuation is studied further. For that purpose, Fig. 6 compares the influence of s and B on $\varepsilon_{v.M.}$. The curved isolines (constant value of $\varepsilon_{v.M.}$) confirm that s has a non-linear and decreasing influence on $\varepsilon_{v.M.}$. The increasingly vertical direction of the isolines for $s > 10\,\mu\mathrm{m}$ demonstrates that in this range of K_{joint} B is the parameter dominating the magnitude of $\varepsilon_{v.M.}$. This finding is also of great importance for the manufacturing process. It shows that once a certain K_{joint} has been achieved in the sintering by $s \approx 10\,\mu\mathrm{m}$ a further increase of K_{joint} has only minor influence on the magnetic response and $\varepsilon_{v.M.}$. Unless other reasons for greater K_{joint} like improved fatigue behaviour exist, resources would not need to be invested on this parameter. The observable pattern in Fig. 6 is independent of f, Timoshenko beam (B31 and B32), and BC. The influence of s on $\varepsilon_{v.M.}$ reaches in each case its maximum at $min(s) = 5\,\mu\mathrm{m}$ and $max(B) = 2.00\,\mathrm{T}$.

From the results of this study, an analytical equation for the relation between $\varepsilon_{v.M.}$ and s can be derived. Fig. 4.e, f plots the increment $d\varepsilon_{v.M.}/ds$ in a log-log-plot. The data gives almost perfectly straight lines. This means that the following equation describes this log-log-relationship [66]:

$$\left[\frac{d\varepsilon_{v.M.}}{ds}\right] = a\,B\,s^b \tag{9}$$

Eq. 9 holds true, irrespectively of f, BC, or Timoshenko beam. a and b are material constants. Regression values for a and b from the values of Fig. 4.e, f are given in Table 5 as obtained for $B = 1\,\mathrm{T}$. The expression $d\varepsilon_{v.M.}/ds$ can be transformed into $\varepsilon_{v.M.}$ by integration along s:

$$\begin{gathered}\varepsilon_{v.M.} = \int \left[\frac{d\varepsilon_{v.M.}}{ds}\right] ds = \int \left(\,a\,B\,s^b\right)\,ds = \frac{1}{b+1}\,a\,B\,s^{b+1} \\ a\,[\mathrm{T}^{-1}\mu\mathrm{m}^{-(\mathrm{b}+1)}],\; b\,[-] \in \mathbb{R}^-\end{gathered} \tag{10}$$

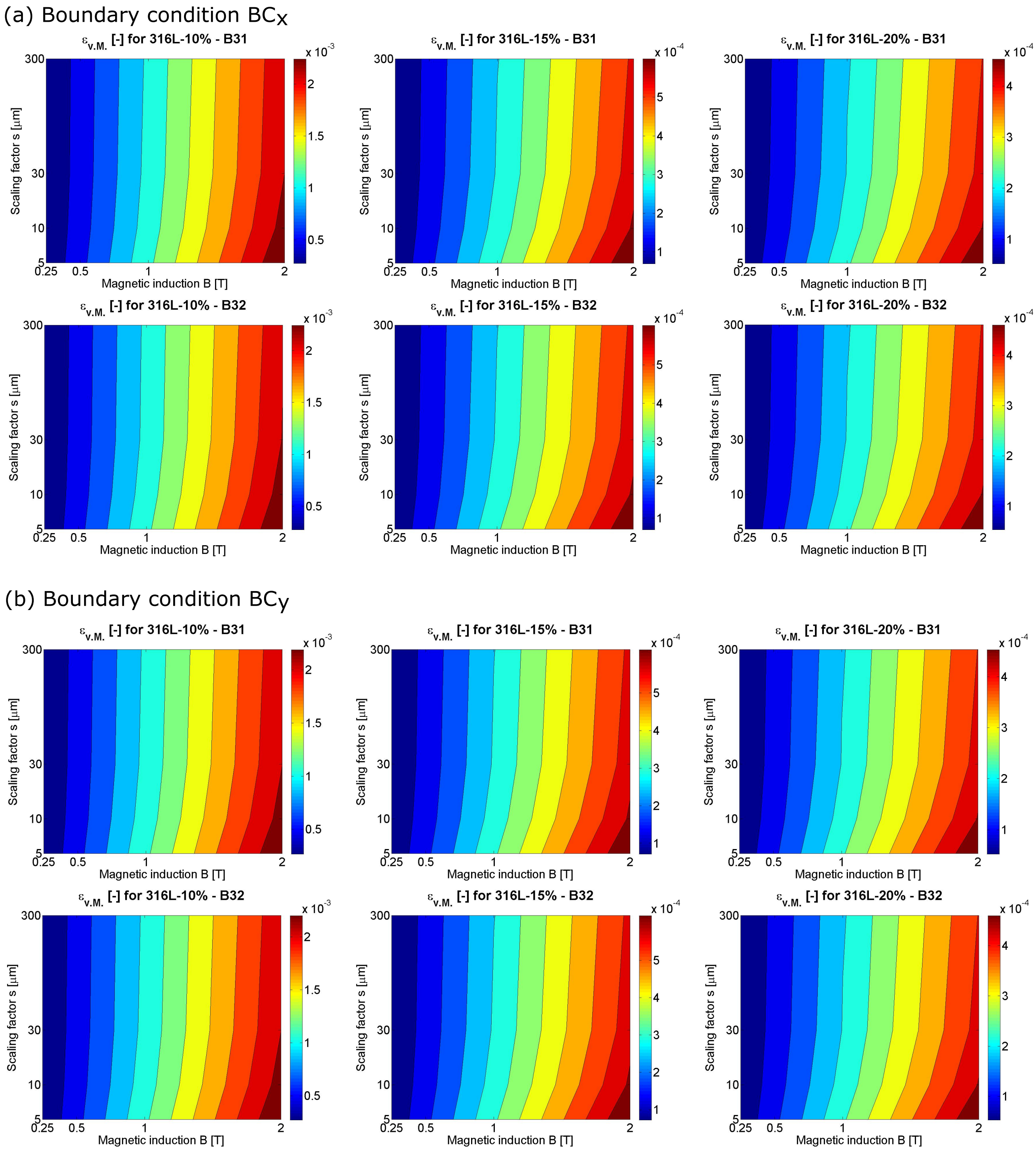

Figure 6: **Parameter study:** Obtained $\varepsilon_{v.M.}$ (averaged for each f) depending on s and B in (a) for $\mathrm{BC_x}$, and (b) for $\mathrm{BC_y}$.

The magnitude of $d\varepsilon_{v.M.}/ds$ and $\varepsilon_{v.M.}$ scales linearly with B. The coefficient of determination r^2 gives proof of the near perfect match with values close to the ideal 1. The importance of Eq. 10 is that for the first time the network strain magnitude under magnetic actuation can be linked by a very simple analytical equation to K_{joint}. Future work will have to investigate what variables define the deformation and strain for amended geometries of fibre network bodies. This will be of particular interest in the planning of experimental procedures involving cell cultures.

Table 5: **Regression analysis:** Values plotted in Fig. 4.e, f leading to $\varepsilon_{v.M.} = \frac{1}{b+1}\, a\, B\, s^{b+1}$ (Eq. 10).

		$\mathbf{BC_x}$			$\mathbf{BC_y}$		
FVF and beam type		a [$\mathrm{T^{-1}\mu m^{-(b+1)}}$]	b [-]	r^2 [-]	a [$\mathrm{T^{-1}\mu m^{-(b+1)}}$]	b [-]	r^2 [-]
$f = 10\%$ for	B31	-2.3092·10^{-4}	-1.5690	0.974	-3.0284·10^{-4}	-1.6420	0.996
	B32	-3.5820·10^{-4}	-1.7250	0.996	-3.0144·10^{-4}	-1.6386	0.996
$f = 15\%$ for	B31	-1.1683·10^{-4}	-1.6294	0.997	-1.2201·10^{-4}	-1.6403	0.999
	B32	-1.1406·10^{-4}	-1.6200	0.996	-1.1279·10^{-4}	-1.6121	0.994
$f = 20\%$ for	B31	-9.3871·10^{-5}	-1.6197	0.996	-9.5253·10^{-5}	-1.6199	0.996
	B32	-9.5028·10^{-5}	-1.6218	0.996	-9.5116·10^{-5}	-1.6181	0.996

Conclusions about FE simulations based on nano-CT images

The obtained 3D deformation fields demonstrate that sintered fibre networks are subjected to complex 3D deformation under magnetic actuation. Regions of compression, tension, and shear can be identified. Equivalent strain measures, such as the von-Mises strain $\varepsilon_{v.M.}$, provide a useful tool for strain field quantification. The deformation patterns discovered in the present study are not the results of uneven material distribution or fibre orientation. Instead, they can be considered a reproducible material feature under magnetic actuation.

This study employs nano-CT as acquisition methodology for 3D images of the samples. Combined with the post-processing [53, 54] employed, it is an efficient tool for the creation of FE meshes. Similar applications of the skeletonisation algorithms, apart from fibre networks, are rock cross sections and the shape of cortical neurons. It is demonstrated that nano-CT allows the efficient acquisition of complex 3D fibre network geometries. The post-processed image stacks are transferable into FE assemblies of more than 1 million elements. Without automated image acquisition, these 3D shapes could not be realised, or at least not at that scale of sample size. In the optimisation of experimental procedures such as prototyping for the application of fibre networks, nano-CT scans provide an important radiological tool.

Increasing fibre density f is shown to reduce the obtained strain at this V. The influence of the size effect is one of the very interesting topics for future research. The influence of the Timoshenko beam interpolation (linear or quadratic) on the strain magnitude matches the respective influence observed for these two beams on the transverse Young's modulus [10].

The deformation is not uniform across the samples under magnetic actuation, unlike what's known for uniaxial mechanical actuation [10]. Local strain peaks are located in the free corners of the sample cubes, independently of the applied BC setting. This has to be taken into consideration for applications of the material in the future. The imposing of a mechanical stimulus for the enhancing of eg bone growth is one potential field in tissue engineering. Controllability and reproducibility of mechanics will be mandatory for this. A reference design point for this is still the experimental work of Rubin from 1985 where he demonstrated periosteal and endothelial bone growth at frequencies of 1.0 Hz cyclical strain of the magnitude 0.001 [50].

A comparison between the influence of the joint stiffness and the influence of the magnetic induction on the strain magnitude demonstrates that the latter one exceeds the first one by far. This implies for the manufacturing or the potential design of machine components including these fibre networks that the joint stiffness is negligible with respect to the magnitude of magnetic induction as long as a minimum joint stiffness is achieved in the sintering step. The non-linear influence of the joint stiffness can be expressed by a simple analytical function which we derive in this study (Eq. 10).

The range of worthwhile future work is manifold. The material stiffness exhibits a distinctive dependency on sample size [10]. This effect would be worth investigating further also under magnetic actuation. The current model neglects mechanical inter-fibre interaction due to the computational demands ($\approx 10^6$ beams per sample). For future studies in particular if of smaller scale, the assignment of surface interaction rules will be of interest. And of course, in-vitro studies which include cell cultures on 3d scaffolds are of interest. Greater controllability of geometry and deformation patterns will be achievable by the use of 3D printed scaffolds [67, 68]. The integration of fibre network scaffolds into vibration bioreactors [69] offers manifold options for the controlled stimulation of tissue. In the field of bone tissue engineering, several future applications could benefit from growth inducing 3D scaffolds. Whether the optimal way for growth stimulation will be mechanically [50] or in other forms that influence cell biology pathways remains to be seen. Bone defect healing after traumatic bone fractures or joint replacement surgery still affects patients [70]. 3D scaffolds have the potential to allow new therapies with greater patient benefit [51]. Metallic fibre networks are one technology option for that. Nano-CT image acquisition in combination with the FE method is a valuable methodology when investigating their local mechanical deformation.

Acknowledgements

The authors wish to thank Dr Garth Wells for his advice about Timoshenko beam types, and boundary conditions. Also Dr Arul Britto is acknowledged for sharing his expertise about model implementation in Abaqus.

Author contributions statement

WAB designed the experiments, WAB conducted the experiment, WAB analysed the results, WAB wrote the manuscript.

Declaration about conflict of interest/funding/ethical approval)

Conflicts of Interest: None. Funding: This research was supported by the European Research Council Grant No 240446 (http://erc.europa.eu/). Ethical Approval: Not required.

Additional information

Competing financial interests. The authors declare no competing financial interests.

[1] GE Sensing & Inspection Technologies GmbH, nanotom - high resolution 3D nanofocus CT, Wunstorf (Germany), 2012.
URL www.phoenix-xray.com

[2] T. W. Clyne, A. E. Markaki, J. C. Tan, Mechanical and magnetic properties of metal fibre networks, with and without a polymeric matrix, Composites Science and Technology 65 (15-16) (2005) 2492–2499.

[3] A. E. Markaki, T. W. Clyne, Magneto-mechanical actuation of bonded ferromagnetic fibre arrays, Acta Materialia 53 (3) (2005) 877–889. doi:10.1016/j.actamat.2004.10.037.
URL http://linkinghub.elsevier.com/retrieve/pii/S1359645404006597

[4] A. E. Markaki, A. W. Justin, A magneto-active scaffold for stimulation of bone growth, Materials Science & Technology 30 (13a) (2014) 1590–1598. doi:10.1179/1743284714Y.0000000579.
URL http://www.maneyonline.com/doi/abs/10.1179/1743284714Y.0000000579

[5] W. A. Bosbach, Mechanical bone growth stimulation by magnetic fibre networks obtained through a competent finite element technique, Scientific Reports 7 (1) (2017) 11109. doi:10.1038/s41598-017-07731-6.

[6] W. A. Bosbach, The mechanical and magnetic behaviour of sintered fibre networks and their suitability for a therapeutic, biomedical application, Ph.D. thesis, University of Cambridge (2015).
URL http://hooke.lib.cam.ac.uk/cgi-bin/bib_seek.cgi?cat=man&bib=42147

[7] M. Z. Jin, C. Q. Chen, T. J. Lu, The mechanical behavior of porous metal fiber sintered sheets, Journal of the Mechanics and Physics of Solids 61 (1) (2013) 161–174.

[8] S. Neelakantan, W. Bosbach, J. Woodhouse, A. Markaki, Characterization and deformation response of orthotropic fibre networks with auxetic out-of-plane behaviour, Acta Materialia 66 (2014) 326–339.

[9] R. L. Spear, B. Srigengan, S. Neelakantan, W. Bosbach, R. A. Brooks, A. E. Markaki, Physical and Biological Characterization of Ferromagnetic Fiber Networks: Effect of Fibrin Deposition on Short-Term In Vitro Responses of Human Osteoblasts, Tissue Engineering Part A 21 (3-4) (2015) 463–474. doi:doi:10.1089/ten.tea.2014.0211.

[10] W. A. Bosbach, The Elastic Behaviour of Sintered Metallic Fibre Networks: A Finite Element Study by Beam Theory, Plos One 10 (11) (2015) e0143011. doi:10.1371/journal.pone.0143011.
URL http://dx.plos.org/10.1371/journal.pone.0143011

[11] W. C. Röntgen, Ueber eine neue Art von Strahlen (Vorläufige Mittheilung), in: Sonderabbdruck der Sitzungsberichte der Würzburger Physik.-medic. Gesellschaft, Würzburg (Germany), 1895.

[12] W. Härer, G. Lauritsch, T. Mertelmeier, Tomographie - Prinzip und Potenzial der Schichtbildverfahren, in: J. Freyschmidt (Ed.), Handbuch diagnostische Radiologie - Strahlenschutz Strahlenbiologie Strahlenschutz, Handbuch diagnostische Radiologie, Berlin/Heidelberg (Germany), 2003, pp. 191–202. doi:10.1007/b137524.
URL http://link.springer.com/10.1007/b137524

[13] M. Buzug, Computed Tomography - From Photon Statistics to Modern Cone-Beam CT, Luebeck (Germany), 2008.

[14] R. C. Picu, Mechanics of random fiber networks - a review, Soft Matter 7 (15) (2011) 6768–6785.

[15] J. Dirrenberger, S. Forest, D. Jeulin, Towards gigantic RVE sizes for 3D stochastic fibrous networks, International Journal of Solids and Structures 51 (2) (2014) 359–376.

[16] D. Rodney, B. Gadot, O. R. Martinez, S. R. du Roscoat, L. Orgéas, Reversible dilatancy in entangled single-wire materials, Nature Materials 15 (2016) 72–77. doi:10.1038/nmat4429.
URL http://www.nature.com/doifinder/10.1038/nmat4429

[17] A. C. Small, J. H. Johnston, Novel hybrid materials of magnetic nanoparticles and cellulose fibers, Journal of Colloid and Interface Science 331 (1) (2009) 122–126. doi:10.1016/j.jcis.2008.11.038.
URL http://dx.doi.org/10.1016/j.jcis.2008.11.038

[18] M. Wang, Q. Kang, N. Pan, Thermal conductivity enhancement of carbon fiber composites, Applied Thermal Engineering 29 (2-3) (2009) 418–421. doi:10.1016/j.applthermaleng.2008.03.004.
URL http://dx.doi.org/10.1016/j.applthermaleng.2008.03.004

[19] M. Wang, J. He, J. Yu, N. Pan, Lattice Boltzmann modeling of the effective thermal conductivity for fibrous materials, International Journal of Thermal Sciences 46 (9) (2007) 848–855. doi:10.1016/j.ijthermalsci.2006.11.006.

[20] M. Faessel, C. Delisée, F. Bos, P. Castéra, 3D modelling of random cellulosic fibrous networks based on X-ray tomography and image analysis, Composites Science and Technology 65 (13) (2005) 1931–1940. doi:10.1016/j.compscitech.2004.12.038.

[21] N. Lippitz, J. Rösler, Damage Behavior of Sintered Fiber Felts, Metals 5 (2) (2015) 591–602. doi:10.3390/met5020591.
URL http://www.mdpi.com/2075-4701/5/2/591/

[22] E. T. Thostenson, T. W. Chou, Carbon nanotube networks: Sensing of distributed strain and damage for life prediction and self healing, Advanced Materials 18 (21) (2006) 2837–2841. doi:10.1002/adma.200600977.

[23] V. P. W. Shim, V. B. C. Tan, T. E. Tay, Modelling deformation and damage characteristics of woven fabric under small projectile impact, International Journal of Impact Engineering 16 (4) (1995) 585–605. doi:10.1016/0734-743X(94)00063-3.

[24] M. M. Mannarino, G. C. Rutledge, Mechanical and tribological properties of electrospun PA 6(3)T fiber mats, Polymer 53 (14) (2012) 3017–3025. doi:10.1016/j.polymer.2012.04.039.

[25] A. Ridruejo, C. González, J. LLorca, A constitutive model for the in-plane mechanical behavior of nonwoven fabrics, International Journal of Solids and Structures 49 (17) (2012) 2215–2229. doi:10.1016/j.ijsolstr.2012.04.014.

[26] F. Farukh, E. Demirci, B. Sabuncuoglu, M. Acar, B. Pourdeyhimi, V. V. Silberschmidt, Mechanical analysis of bi-component-fibre nonwovens: Finite-element strategy, Composites Part B: Engineering 68 (2015) 327–335. doi:10.1016/j.compositesb.2014.09.003.

[27] R. Y. Kwon, A. J. Lew, C. R. Jacobs, A microstructurally informed model for the mechanical response of three-dimensional actin networks, Computer Methods in Biomechanics and Biomedical Engineering 11 (4) (2008) 407–418.

[28] O. Lieleg, K. M. Schmoller, M. M. A. E. Claessens, A. R. Bausch, Cytoskeletal polymer networks: viscoelastic properties are determined by the microscopic interaction potential of cross-links, Biophysical journal 96 (11) (2009) 4725–4732.

[29] H. Yamaoka, S. Matsushita, Y. Shimada, T. Adachi, Multiscale modeling and mechanics of filamentous actin cytoskeleton, Biomechanics and modeling in mechanobiology 11 (3) (2012) 291–302.

[30] H. Cox, The elasticity and strength of paper and other fibrous materials, British Journal of Applied Physics 3 (3) (1951) 72–79.

[31] M. Alava, K. Niskanen, The physics of paper, Reports on Progress in Physics 69 (3) (2006) 669–723.

[32] J. A. Astrom, J. P. Makinen, H. Hirvonen, J. Timonen, Stiffness of compressed fiber mats, Journal of Applied Physics 88 (9) (2000) 5056–5061.

[33] D. A. Head, F. C. MacKintosh, A. J. Levine, Nonuniversality of elastic exponents in random bond-bending networks, Physical Review E 68 (2) (2003) 025101(R). doi:10.1103/PhysRevE.68.025101.

[34] C. P. Broedersz, M. Sheinman, F. C. MacKintosh, Filament-Length-Controlled Elasticity in 3D Fiber Networks, Physical Review Letters 108 (7) (2012) 078102.

[35] A. S. Shahsavari, R. C. Picu, Size effect on mechanical behavior of random fiber networks, International Journal of Solids and Structures 50 (20-21) (2013) 3332–3338.

[36] P. Ducheyne, L. Hench, The processing and static mechanical properties of metal fibre reinforced bioglass, Journal of Materials Science 17 (2) (1982) 595–606.

[37] D. Taylor, F. Clarke, B. McCormack, J. Sheehan, Reinforcement of Bone Cement Using Metal Meshes, Journal of Engineering in Medicine 203 (1) (1989) 49–53. doi:10.1243/PIME.

[38] S. P. Kotha, C. Li, S. R. Schmid, J. J. Mason, Fracture toughness of steel-fiber-reinforced bone cement., Journal of biomedical materials research. Part A 70A (3) (2004) 514–521. doi:10.1002/jbm.a.30107.
URL `http://www.ncbi.nlm.nih.gov/pubmed/15293326`

[39] S. Kim, C. Sioutas, M. Chang, Electrostatic Enhancement of the Collection Efficiency of Stainless Steel Fiber Filters, Aerosol Science and Technology 32 (3) (2010) 197–213.

[40] I. O. Golosnoy, A. Cockburn, T. W. Clyne, Optimisation of Metallic Fibre Network Materials for Compact Heat Exchangers, Advanced Engineering Materials 10 (3) (2008) 210–218. doi:10.1002/adem.200800021.
URL `http://doi.wiley.com/10.1002/adem.200800021`

[41] C. Veyhl, T. Fiedler, O. Andersen, J. Meinert, T. Bernthaler, I. Belova, G. Murch, On the thermal conductivity of sintered metallic fibre structures, International Journal of Heat and Mass Transfer 55 (9-10) (2012) 2440–2448. doi:10.1016/j.ijheatmasstransfer.2012.01.016.
URL `http://linkinghub.elsevier.com/retrieve/pii/S0017931012000178`

[42] R. H. Marchessault, P. Rioux, L. Raymond, Magnetic cellulose fibres and paper: preparation, processing and properties, Polymer 33 (19) (1992) 4024–4028. doi:10.1016/0032-3861(92)90600-2.

[43] R. Satcher, F. Dewey, Theoretical estimates of mechanical properties of the endothelial cell cytoskeleton, Biophysical Journal 71 (1) (1996) 109–118.

[44] D. Head, A. Levine, F. MacKintosh, Distinct regimes of elastic response and deformation modes of cross-linked cytoskeletal and semiflexible polymer networks, Physical Review E 68 (6) (2003) 061907.

[45] A. R. Bausch, K. Kroy, A bottom-up approach to cell mechanics, Nature Physics 2 (4) (2006) 231–238.

[46] W. J. Li, C. T. Laurencin, E. J. Caterson, R. S. Tuan, F. K. Ko, Electrospun nanofibrous structure: A novel scaffold for tissue engineering, Journal of Biomedical Materials Research 60 (4) (2002) 613–621. doi:10.1002/jbm.10167.

[47] T. Mammoto, D. E. Ingber, Mechanical control of tissue and organ development., Development 137 (9) (2010) 1407–1420. doi:10.1242/dev.024166.

[48] B. Hashmi, L. D. Zarzar, T. Mammoto, A. Mammoto, A. Jiang, J. Aizenberg, D. E. Ingber, Developmentally-inspired shrink-wrap polymers for mechanical induction of tissue differentiation, Advanced Materials 26 (20) (2014) 3253–3257. doi:10.1002/adma.201304995.

[49] F. P. Melchels, M. A. Domingos, T. J. Klein, J. Malda, P. J. Bartolo, D. W. Hutmacher, Additive manufacturing of tissues and organs, Progress in Polymer Science 37 (8) (2012) 1079–1104. doi:10.1016/j.progpolymsci.2011.11.007.
URL `http://linkinghub.elsevier.com/retrieve/pii/S0079670011001328`

[50] C. T. Rubin, L. E. Lanyon, Regulation of bone mass by mechanical strain magnitude, Calcified tissue international 37 (4) (1985) 411–417.
URL `http://www.ncbi.nlm.nih.gov/pubmed/3930039`

[51] Z. Lei, Y. Guojing, J. Blake N., J. Xiaofeng, Three-dimensional (3D) printed scaffold and material selection for bone repair, Acta Biomaterialia 84 (2019) 16–33.

[52] Dassault Systèmes, Abaqus 6.13 Online Documentation (2013).
URL `http://dsk.ippt.pan.pl/docs/abaqus/v6.13/index.html`

[53] T. C. Lee, R. L. Kashyap, C. Chong-Nam, Building Skeleton Models via 3-D Medial Surface/Axis Thinning Algorithms, Graphical Models and Image Processing 56 (6) (1994) 462–478.

[54] W. B. Lindquist, 3DMA General Users Manual, Stony Brook (USA), 1999.

[55] H. Yang, A Geometric and Statistical Analysis of Fibrous Materials from Three-Dimensional High Resolution Images, Ph.D. thesis, State University of New York at Stony Brook (2001).

[56] D. Gross, W. Hauger, J. Schröder, W. A. Wall, J. Bonet, Engineering Mechanics 2: Mechanics of Materials, Heidelberg (Germany), 2011.

[57] S. Timoshenko, On the Correction for Shear of the Differential Equation for Transverse Vibrations of Prismatic Bars, Philosophical Magazine Series 6 41 (245) (1921) 744–746.

[58] S. Timoshenko, On the transverse vibrations of bars of uniform cross-section, Philosophical Magazine Series 6 43 (253) (1922) 125–131.

[59] Dassault Systèmes, Abaqus Analysis User's Guide 29.3.3 Choosing a beam element (2013).
URL `http://129.97.46.200:2080/v6.13/books/usb/default.htm?startat=pt06ch29s03alm08.html`

[60] Dassault Systèmes, Abaqus Theory Guide 1.5.1 Equilibrium and virtual work (2013).
URL `http://129.97.46.200:2080/v6.13/books/stm/default.htm?startat=ch01s05ath08.html`

[61] J. D. Logan, Applied Mathematics, 6th Edition, Lincoln, Nebraska (USA), 2006.

[62] P. J. Atzberger, Stochastic Eulerian Lagrangian methods for fluid–structure interactions with thermal fluctuations, Journal of Computational Physics 230 (8) (2011) 2821–2837. doi:10.1016/j.jcp.2010.12.028.

[63] D. Azarnykh, S. Litvinov, N. A. Adams, Numerical methods for the weakly compressible Generalized Langevin Model in Eulerian reference frame, Journal of Computational Physics 314 (2016) 93–106. doi:10.1016/j.jcp.2016.02.073.
URL `http://linkinghub.elsevier.com/retrieve/pii/S0021999116001558`

[64] W. Hosford, Mechanical behavior of materials, 2nd Edition, New York (USA), 2010.

[65] L. Alting, Manufacturing engineering processes, 2nd Edition, Lyngby (Denmark), 1994.

[66] Wolfram Alpha, LogLogPlot (http://reference.wolfram.com/language /ref/LogLogPlot.html - 06 Oct 2016).
URL `http://reference.wolfram.com/language/ref/LogLogPlot.html`

[67] H. Yuan, K. Xing, H. Y. Hsu, Trinity of three-dimensional (3D) scaffold, vibration, and 3D printing on cell culture application: A systematic review and indicating future direction, Bioengineering 5 (3) (2018). doi:10.3390/bioengineering5030057.

[68] J. Deering, A. Presas, B. E. Lee, D. Valentín, B. Yu, C. Heiss, K. Grandfield, W. A. Bosbach, Response of Saos-2 Osteoblast-like Cells to Kilohertz-Resonance Excitation in Porous Metallic Scaffolds, Journal of the Mechanical Behavior of Biomedical Materials 106 (103726) (2020).

[69] D. Valentin, C. Roehr, A. Presas, C. Heiss, E. Egusquiza, W. A. Bosbach, Experimental-Numerical Design and Evaluation of a Vibration Bioreactor using Piezoelectric Patches, Sensors 19 (2) (2019) 436. doi:https://doi.org/10.3390/s19020436.

[70] G. Bowden, M. McNally, S. Thomas, A. Gibson (Eds.), Oxford Handbook of Orthopaedics and Trauma, repr. 2013 Edition, Oxford (UK), 2010.